Heat and Fluid Flow in an Optical Switch Bubble

John J. Uebbing, Stephan Hengstler, *Member, IEEE*, Dale Schroeder, Shalini Venkatesh, *Member, IEEE*, and Rick Haven

***Abstract*—The Agilent all-optical bubble switch uses bubbles in an organic fluid index matched to a silica planar lightwave circuit. The bubble is created and sustained by heaters that are deposited on an attached silicon substrate. Testing of the bubble shows how heater power and ambient pressure affect bubble shape, size, and optical reflection characteristics. Heat and fluid flow in the bubble were modeled in 2D and 3D using the homogeneous bubble model in the Flow3D modeling software. Fluid condensing on the trench wall causes a dimple on the bubble and hence nonoptimum optical reflection. To aid understanding, the bubble, silica walls, and heaters were also modeled as a thermal resistance network. Because the pressure drop across the bubble wall is fixed, the bubble size is determined by $P_{res}/\Delta T_t$, where P_{res} is the heater power and ΔT_t is the temperature difference between the bubble and the substrate. Heating the trench walls beyond the bubble temperature with heaters located underneath the trench wall will dry out the trench wall and give a stable optical reflection. As ΔT_t approaches zero, a bubble is sustained without any heater power and with zero fluid flow. This "static" bubble provides for a very stable optical reflection. [1453]**

***Index Terms*—Bubbles, fluidics, optical switches, microactuators, microelectromechanical devices, resistance heating.**

I. Introduction

THE Agilent Optical Bubble Switch was developed for use as a optical cross connect for deployment at the nodes of all-optical switched telecom networks. As light reflectors, it uses vapor bubbles confined to trenches in a waveguide array. In contrast to the inkjet bubble, the optical switch bubble is on continuously during operation. Continuous operation means that the fluid flow is continuous, heaters dissipate power continuously, and inertia effects are only noticeable during turn on and turn off. The objective of the work presented here was to

1) understand the basic energy and material flow in the bubble;
2) characterize the optical reflection properties of the bubble and their dependence on other bubble properties;
3) find means to obtain a stable optical reflection.

The paper is organized as follows. In Section II, we begin with a system description of the Optical Bubble Switch and its principle of operation. Section III discusses the heat flow patterns within the switching cell. The following section introduces the useful concept of bubble thermal transconductance. Details on fluid dynamics modeling with the Flow3D finite difference software package are given in Section V. In Section VI, we present one of the main results of our research—the discovery of a thin liquid film on the reflecting bubble wall. Section VII explains the dependence of reflected signal power on bubble shape and size followed by a brief excursion into bubble instability. Subsequently, Section IX describes drywall operation, which eliminates the liquid film on the reflecting sidewall. A switch bubble may also be sustained at zero heater power as the derivation in Section X reveals. Finally, in Section XI, we summarize the main results of our research.

Manuscript received November 3, 2004; revised June 6, 2006. Subject Editor F. K. Forster.

J. J. Uebbing is with Spudnik, Inc., San Jose, CA 95134 USA (e-mail: juebbing@spudnikinc.com).

S. Hengstler is with the Biosensor Solutions Division, Avago Technologies, San Jose, CA 95131 USA (e-mail: stephan.hengstler@avagotech.com).

D. Schroeder and R. Haven are with Agilent Technologies, Santa Clara, CA 95052 USA.

S. Venkatesh is with the U.S. Advanced R&D Center, Avago Technologies, San Jose, CA 95131 USA.

Digital Object Identifier 10.1109/JMEMS.2006.883529

II. Description of the Bubble Switch

A. Layout

Fig. 1 shows a top view of a switching cell in Agilent's Optical Switch. The input optical signals travel in an array of waveguides fabricated on a fused silica substrate. 15-μm-wide trenches for containing the switching bubbles are etched into the resulting planar lightwave circuit (PLC) at the cross points. The attached silicon substrate called the matrix controller chip (MCC) has a 32×32 array of small side or center heaters located beneath each cross point. The resistive heaters are made of tantalum aluminum alloy and their 0.08 μm thick active heating area measures 6×40 μm. Without a bubble present in the trench, the light can travel unimpeded from "IN" to "DROP" port and from "ADD" to "OUT" port.

Fig. 2 shows a cross-sectional view of the trench, the bubble, and the side heater elements. The material stack consists of a silicon substrate at the bottom, a silicon dioxide passivation layer containing the resistive side heaters, a 5-μm fluid-filled gap, and the silica substrate with trench and waveguides on top. Conductive gold pillows are located above each side heater resistor to spread the heat more uniformly.

The trench wall has a slight tilt angle to it as a result of the etching process used to form it. Initially, only a single center heater was used. Later we used only the side heaters. The side heaters allow operating at a lower heater temperature due to their superior heat transfer characteristics. As will be discussed in this paper, they tend to dry out the trench walls during operation. Otherwise, the bubble properties with both heater types are very similar. In this paper, most references will be to operation with side heaters.

B. Switch Operation

The switch operates when a bubble is created in the trench. To visualize the geometries involved, Fig. 3 shows a side view of the long side of an actual bubble with center heater only and Fig. 4 gives a top view photomicrograph of a bubble with

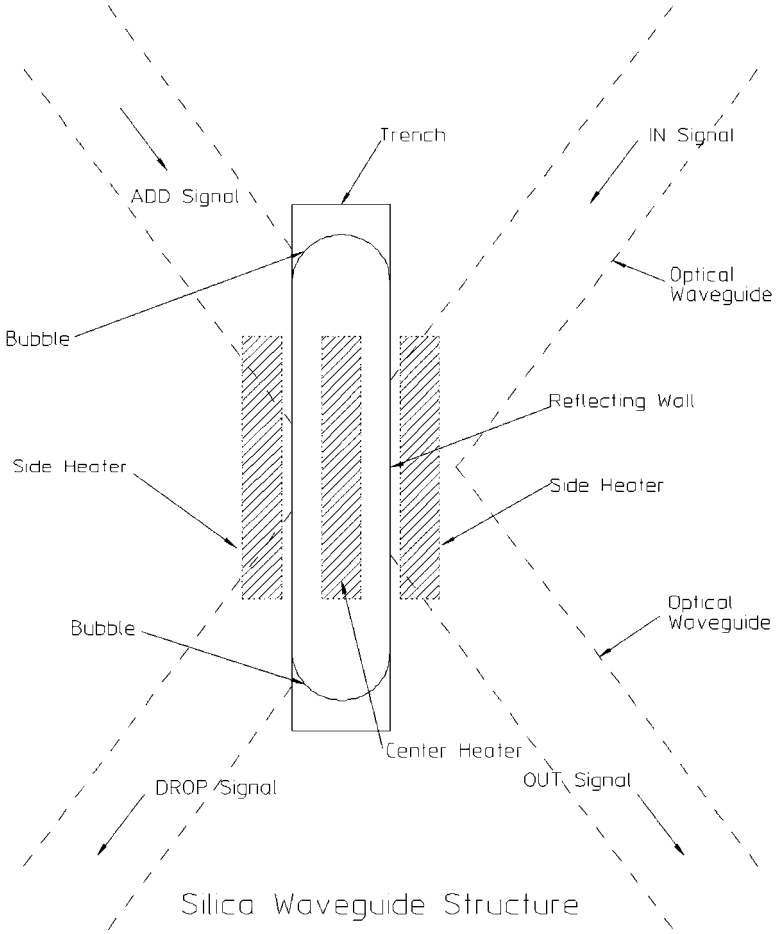

Fig. 1. Top view of switching cell.

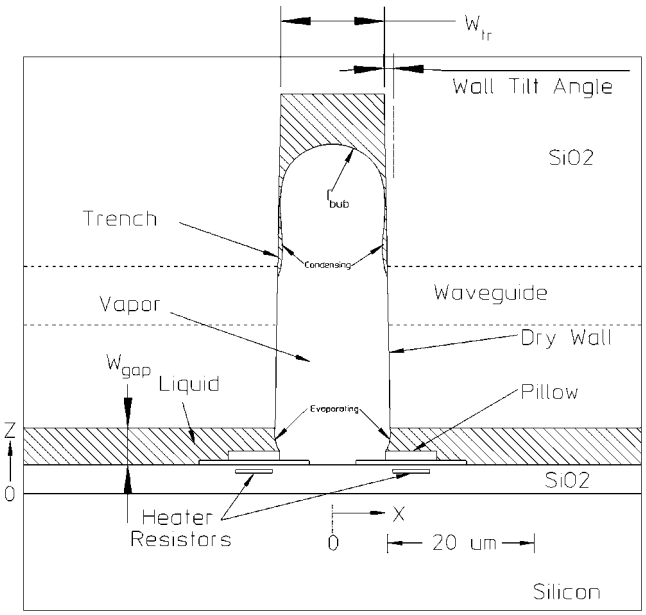

Fig. 2. Cross-sectional view of side heater-type switching cell.

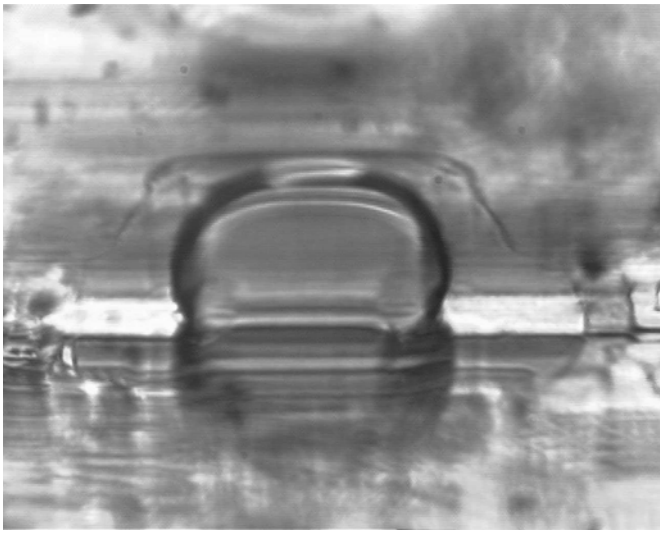

Fig. 3. Side view photomicrograph of a bubble with center heater.

side heaters. In these small bubbles, the only reliable nucleation process is homogeneous nucleation. This occurs when the liquid reaches about 88% of its critical temperature [1].

When a bubble is present in the trench, light from the incoming waveguide or "IN" port is reflected by total internal reflection at the trench wall-bubble vapor interface into the "OUT" port. Light incident at the "ADD" port is reflected back and hence blocked due to asymmetric trench centering across the waveguide crossing. When the bubble collapses, the trench completely fills with index matching liquid and light may travel from the "IN" port freely through the trench into the "DROP" port and similarly from "ADD" to "OUT" port.

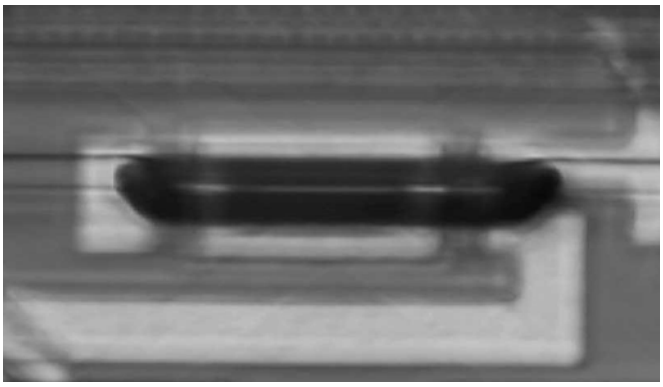

Fig. 4. Top view photomicrograph of a bubble with side heaters.

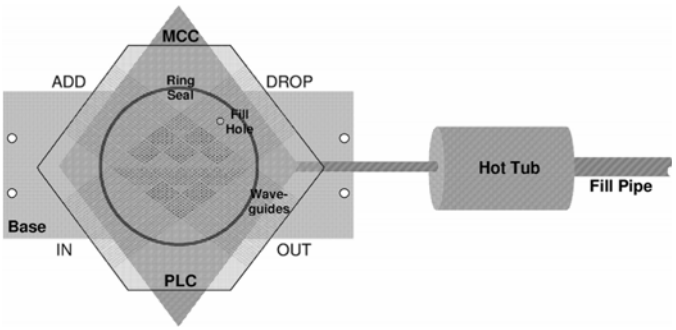

Fig. 5. Device assembly of Agilent's Bubble Switch.

The bubble is maintained by evaporating liquid from the region near the heater. The resultant vapor maintains a pressure inside the bubble that is $\sigma/r_{\rm bub}$ higher than that of the surrounding liquid. σ is the surface tension of the fluid and $r_{\rm bub}$ is the cylindrical radius of the edge of the captured bubble. The hot vapor in the bubble condenses on the walls of the bubble establishing a circulating flow of fluid. This is very similar to the bubble flow patterns described by Chen *et al.* [2], referenced in [3], and much like those shown in [4].

C. Device Assembly

Fig. 5 shows the device assembly of Agilent's Bubble Switch. The MCC substrate is mounted on a molybdenum base plate. A solder ring seal connects MCC and PLC leaving the gap for the fluid. The optical ports "IN," "OUT," "ADD," and "DROP" are accessible at the four faces of the diamond-shaped PLC. A small pipe connects the base plate to an external fluid reservoir called the hot tub. This hot tub can be filled with fluid using a separate fill pipe. We usually fill it to 2/3 fluid and 1/3 vapor space. This provides the volume necessary to expand and collapse the switching bubbles. In our experiments, the hot tub was filled with degassed 2-Fluorotoluene, which establishes an excellent optical index match to the waveguide. A single fill hole—a through hole in the MCC—allows fluid from the hot tub to enter the device, more precisely the 5 μm gap between MCC and PLC. The hot tub supplies fluid to all $32 \times 32 = 1024$ switching cells of the bubble switch.

Thermo-electric coolers control the temperature of the base plate and hot tub separately. Forcing a positive temperature difference between hot tub and device will expand the vapor space inside the hot tub and fill the device with fluid establishing constant fluid pressure across all switching cells. In our experiments, a difference of 10 K typically yields the best compromise between heater power required to sustain a switch bubble and bubble collapse time. The higher the fluid pressure is, the faster the bubbles will collapse at the expense of increased heater power for bubble operation.

D. Optical Performance

The design of Agilent's Bubble Switch was mainly driven by meeting a set of optical performance specifications, which are summarized in Table I in the Appendix. These specifications reflect what was considered a compelling and competitive product for the optical switching market. However, during design and characterization of the switch we encountered difficulties in simultaneously meeting the insertion loss and stability requirements of 8.5 dB and 0.5 dB, respectively. Note that insertion loss is defined as the loss in optical power caused by inserting the optical switch into the signal path. More specifically, depending on the heater power applied, a switching cell would either attain an insertion loss below 7 dB with a stability of 5 dB or achieve a stability of 0.25 dB at an insertion loss above 10 dB. Above all, this dilemma triggered the research and investigation presented in the sections to follow.

III. Bubble Energetics

A. Basic Heat Flow Patterns and Thermal Resistances

Fig. 6 shows a thermal profile of a device with side heaters. This data was obtained from a two-dimensional Flow3D model. The computer model, which is more extensively discussed in Section V, uses the homogeneous bubble model. This model assumes that the bubble temperature and pressure are uniform throughout the bubble. More accurate modeling and [6] have shown this to be a good assumption. Most of the heat flows directly down into the silicon substrate. The evaporating meniscus uses from 2% to 3% of the total heater power to generate the vapor that maintains the bubble. When the heater is located directly underneath the walls of the trench, a fair amount of the heat travels up the sides of the trench wall. This heat can have a significant influence on the optical properties of the bubble as it may dry out the wall at the waveguide location. In this example, the trench wall is hotter than the bubble in the lower or dry region of the wall.

B. Evaporation and Condensation

Evaporative flux in the bubble is modeled in Flow3D® as a function of temperature and pressure jumps at the interface according to the expression

$$\dot{m} = C\sqrt{\frac{M}{2\pi R}}\left(\frac{P_l^{\rm sat}}{\sqrt{T_{\rm liq}}} - \frac{P_v}{\sqrt{T_v}}\right), \tag{1}$$

where $T_{\rm liq}$ denotes the liquid temperature and $P_l^{\rm sat}$ the saturation pressure of the liquid at its temperature. T_v and P_v refer to the vapor temperature and pressure. M is the molecular weight

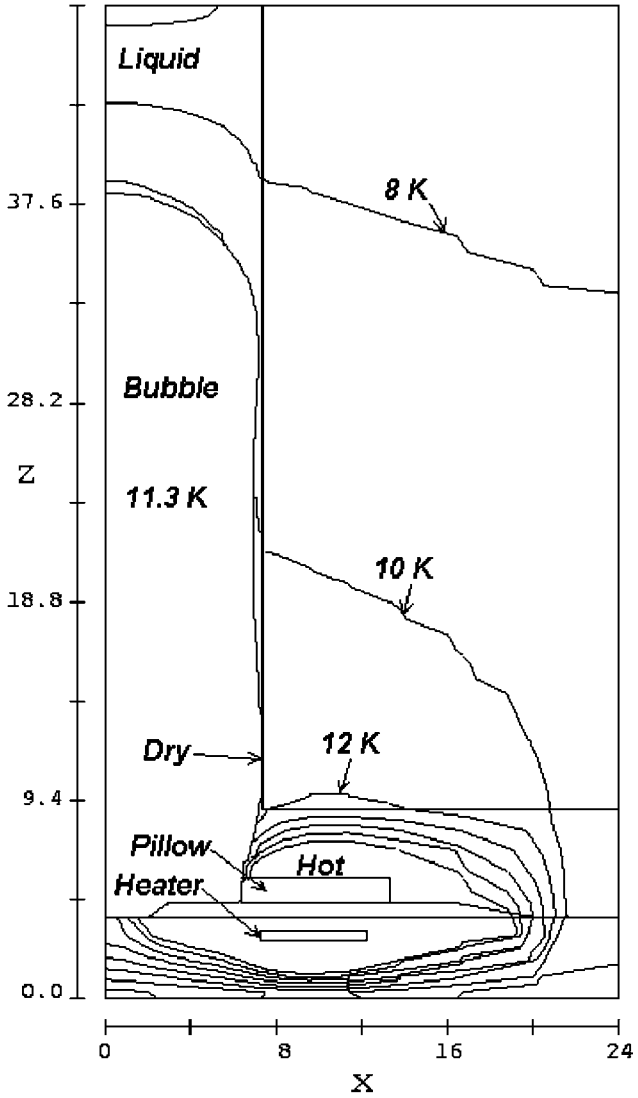

Fig. 6. Bubble thermal profile with side heaters. Distances are in μm, temperatures are in K above $T_{\rm sub}$.

and R is the gas constant. C is called the net accommodation coefficient. For perfect molecular accommodation, C equals 2. Simulations with different accommodation coefficients show that the resulting evaporative flux is not very sensitive to the value of C. The reason is that the limit to the rate of evaporation is determined more by the rate at which heat can be supplied by thermal conduction through the liquid rather than by the rate as determined by (1). The liquid surface temperature $T_{\rm liq}$ and the corresponding $P_l^{\rm sat}$ adjust to accommodate the thermal conduction rate. C was set to 2 in all the device models. $T_{\rm liq}$ and the corresponding $P_l^{\rm sat}$ vary along the surface of the bubble. They take on high values in the evaporative area near the heater and low values in the upper condensing areas. Flow3D does use the above model to calculate vaporization and condensation along an isothermal bubble.

C. Heat Transfer to the Bubble

The simplest way to model heat transfer from the liquid to the bubble is to use a heat transfer coefficient. This coefficient can be worked out from (1) using tabulated fluid properties

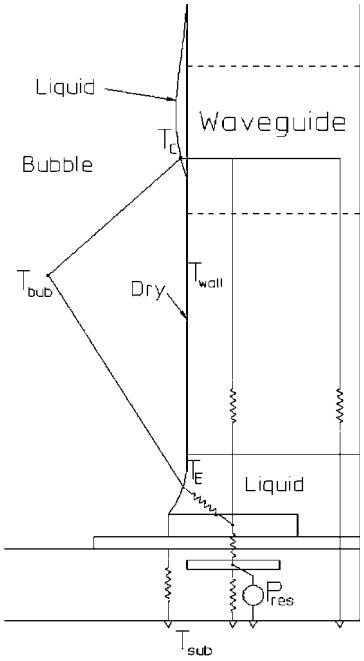

Fig. 7. Thermal resistance model with side heaters.

and measured pressure and temperature values. It is about 1.5 MW/(m^{2}K) in Agilent's bubble-switching cell. As Prosperetti and Plesset [6] have shown, the bubble can be modeled as having a uniform pressure and temperature. The bubble acts as a heat pipe, and for simplicity the heat/mass transfer from liquid to vapor and vapor to liquid can be modeled by assuming perfect conduction inside the bubble, with heat transfer limited by the heat transfer coefficient and thermal conduction in the liquid. In the dry areas of the bubble wall, heat transfer can occur by gas phase conduction. Under normal operating conditions, this heating is small compared to the effects of vapor condensation. At very high heater powers and low hot tub temperatures, there is no liquid near the heater and the walls become dry due to vapor phase conduction. This regime is called the "Super Bubble." This regime is not a useful mode of operation because of poor heater life and long bubble collapse times.

D. Thermal Impedance and Mutual Impedance

For purposes of a more intuitive, but less detailed understanding of the heat flow, we also used the simpler thermal resistance model shown in Fig. 7. The figure shows a close-up of the region near the side heater. This model gives a picture of the heat flow in the vapor, fluid, and solid. For example, the wall is heated both by heat flowing up the wall and by vapor condensing on the wet part of the wall. Actual thermal resistance values for a fixed bubble shape can be extracted from finite difference simulations. The most important use of this model lies in providing a framework for considering heater to bubble thermal transconductance.

IV. Approximate Heat and Vapor Flow, Normalization by ΔT_t

As discussed in the previous section, the bubble itself can be modeled as a region of uniform temperature with heat and vapor

flowing into and out of it. Using the thermal resistance network model, the bubble temperature is given by

$$T_{\rm bub} = T_{\rm sub} + \frac{P_{\rm res}}{\Gamma_{\rm bub}(s)} \tag{2}$$

or

$$\Gamma_{\rm bub}(s) = \frac{P_{\rm res}}{T_{\rm bub} - T_{\rm sub}}, \tag{3}$$

where $\Gamma_{\rm bub}(s)$ denotes the mutual thermal transconductance between bubble and heater, $T_{\rm bub}$ is the bubble temperature, $T_{\rm sub}$ the substrate temperature, and $P_{\rm res}$ the heater power. $\Gamma_{\rm bub}(s)$ can vary by 50% as a function of bubble size and shape.

We can also express the heater to bubble thermal transconductance as

$$\Gamma_{\rm bub}(s) = \frac{P_{\rm res}}{\Delta T_t} \tag{4}$$

and alternatively refer to it as the normalized heater power. In this equation

$$\Delta T_t = T_{\rm bub} - T_{\rm sub} \tag{5}$$

and

$$\Delta T_t = T_{\rm ht} + T_\sigma - T_{\rm sub} \tag{6}$$

where $T_{\rm ht}$ denotes the hot tub temperature and T_σ is defined as the change in temperature required to produce a vapor pressure change sufficient to overcome the pressure difference between the inside and the outside of the bubble. Surface tension σ acting over the cylindrical radius of the bubble edge causes this pressure difference. By using the Clausius–Clapeyron equation, we may approximate T_σ by

$$T_\sigma \cong \frac{2\sigma R T_{\rm bub}^2}{p_{\rm bub} h_{fg} W_{\rm tr}}. \tag{7}$$

Here, $p_{\rm bub}$ refers to the bubble pressure, h_{fg} is the enthalpy of evaporation, and $W_{\rm tr}$ the trench width. ΔT_t is also the difference between the actual substrate temperature and the minimum substrate temperature that will support a static bubble (see Section X). The factor of 2 is used because the bubble radius is one half the trench width. This normalized heater power experimentally tracks bubble size and specific features in the optical reflection signal versus heater power curve. These features are discussed in more detail in Section VII.

V. Finite Difference Computer Fluid Dynamics

As mentioned previously, we modeled the bubble using the Flow3D finite difference software package. The trenches etched in fused silica were modeled as fused quartz. The fluid, namely 2-Fluorotoluene, itself required twelve different parameters to specify it properly. These are listed in Table III in the Appendix. The homogeneous bubble model, e.g., uniform pressure and temperature inside the bubble, enabled us to model the bubble to our satisfaction. One of the numerical issues is modeling of the contact line, where liquid, vapor, and solid interface meet. A number of authors [5], [7] have devoted a lot of attention to the fine details of very thin liquid films in these transition regions. Flow3D simply balances forces and fluxes in such boundary cells. Flow3D produces the shape of the bubble surface near the contact line that agrees with our experimental observations. An example of an observed and a simulated bubble are shown in Figs. 3 and 11, respectively.

A. 2D and 3D Simulations

During operation, fluid evaporates from a zone near the heater and condenses on the sides and top of the bubble. The condensing fluid flows alongside the shorter trench walls back to the evaporation zone. In the 2D model, we assume that fluid flows in from the sides at the bottom and flows out at the top of the trench, which is appropriately modeled by constant pressure boundary conditions. In reality these flows are accommodated by significant, but low pressure drop, flows in the third dimension. Very misleading results are obtained if an area is blocked in the 2D model that actually carries fluid flow in the 3D world. 3D modeling is computationally very intensive but does handle the end effects correctly. Under the boundary conditions as mentioned above, 2D models give results in close agreement with equivalent 3D models. In the remainder, we will refer to Flow3D® simulation results at some length.

A 2D Flow3D simulation of the liquid velocity field with center heater is shown in Fig. 8. Surprisingly, it reveals the existence of two evaporation-condensation vortices at the top of the bubble that are symmetric to the bubble vertical axis. Vapor condenses at the very top of the bubble and fluid evaporates at the top of the bubble in proximity to the trench walls.

The authors strongly regret that an equivalent graph of Fig. 6 for the center heater configuration and of Fig. 8 for the side heater configuration could not be recreated since their Flow3D license had expired.

VI. Fluid on the Trench Wall

The single most important outcome of our research is the discovery of a dimple in the bubble shape. The qualitative model of the bubble shape drawn in Fig. 9 illustrates the dimple and its reflective properties as the bubble height varies. It provided the explanation for the mysterious decrease in reflected light power with increasing bubble height, which is given in Section VII in more detail. Figs. 8, 10, and 11 show the dimple on the surface of the bubble. It is very difficult to observe the dimple visually, but it can be seen under certain lighting conditions and inferred from optical loss measurements.

A. Capillarity

The dimple is caused by capillarity. What happens is that the condensing fluid piles up on the wall of the bubble. It tries to escape through the thin film of liquid on the wall of the trench. To push liquid through such a thin layer requires a significant pressure difference. Simulations have shown 3000 Pa of pressure difference between the center and edge of the dimple. The high pressure in the center of the bubble wall causes the bubble to form a dimple. The extent of dimple formation is governed by the capillarity number, defined as

$$\mathrm{Ca} = \frac{3\dot{m}\nu}{\sigma} \cong 75 \times 10^{-6} \tag{8}$$

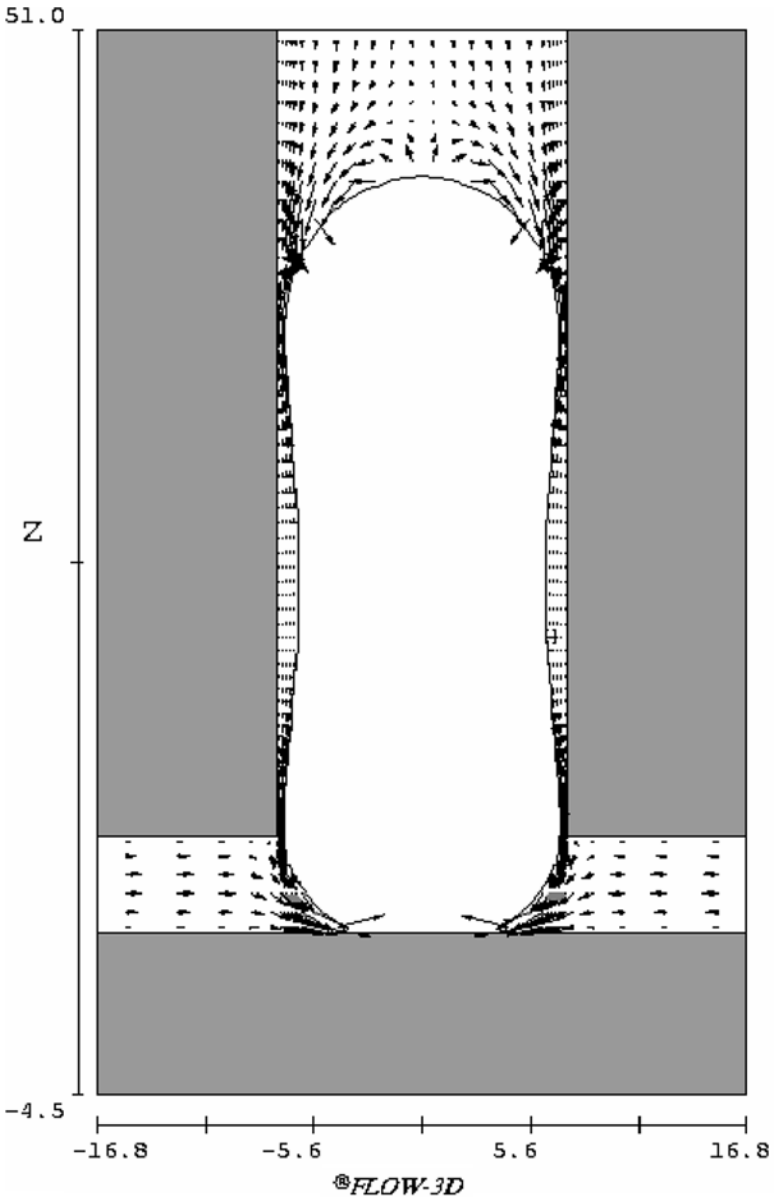

Fig. 8. 2D liquid velocity field with center heater. Dimensions are in μm.

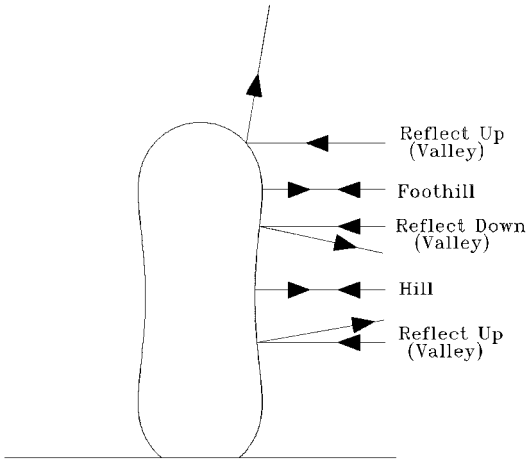

Fig. 9. Hill and valley model with dimple.

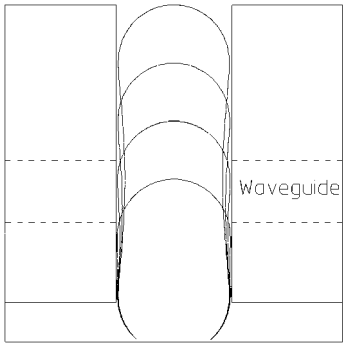

Fig. 10. Lubrication model of dimples, $\mathrm{Ca} = 75 \times 10^{-6}$.

where ν denotes the kinematic viscosity, $\dot{m}$ the condensing mass flux density, and σ is the surface tension. A sixth-order, nonlinear differential equation described by DasGupta *et al.* [5] and by Homsy and Ajaev [7] can be solved to obtain the shape of the vapor-liquid interface. This equation balances viscous and surface tension forces. We numerically integrated the lubrication model equation without approximating the curvature by the second derivative of the fluid thickness. Fig. 10 shows a series of numeric solutions of the dimple shape for different bubble sizes

Fig. 11. 3D view of the dimple model.

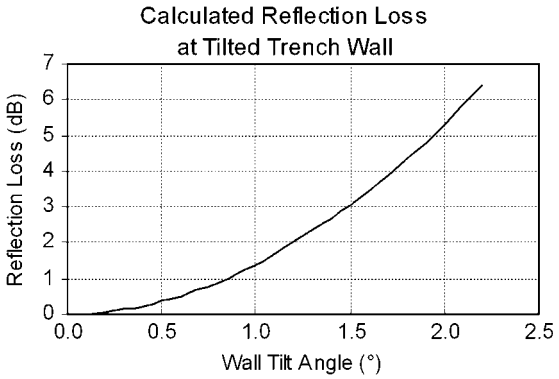

Fig. 12. Reflected signal loss versus mirror wall angle.

under conditions of constant condensing flux density. Fig. 8 shows the fluid flow in a 2D device model.

B. Sensitivity to Waveguide Wall Angle

The fluid build-up on the walls is quite noticeable in the reflected optical signal. The acceptance angle for the reflected light into the optical waveguides is fairly low since the waveguide has an optical numerical aperture (NA) of only 0.055. This means that if the silica reflecting wall of the bubble is not perfectly vertical, the light will not be fully reflected into the waveguide of the "OUT" port resulting in optical power loss. Fig. 12 quantifies this effect as the calculated reflected signal power loss increases with trench wall tilt angle, which directly translates into reflection losses for tilted bubble walls.

From Fig. 10, we see that as the power into the bubble and hence the bubble size varies, the reflecting wall of the bubble at the waveguide location will change angle. Thus, we expect the optical power loss to change with bubble size; different dimple geometries will cause varying amounts of light to escape the waveguide structure. Fig. 13 provides experimental confirmation. It shows two experimental sets of normalized optical signal power vs. heater power curves—one representing the light reflected back into the waveguide and the other the light that is being reflected upwards from the waveguide. Clearly, as a result of the dimple moving across the waveguide location, the back-reflected light attains a minimum ("Valley") when the up-reflected light takes on a maximum.

The correlation between the bubble model of Fig. 9 and the "blow curves," which we call plots of normalized reflected optical signal power versus heater power, of Fig. 13 is our best experimental evidence for the dimple in the bubble wall. The thickness of the fluid layer at the dimple's center is in the order of 1 μm. It is very difficult to observe the dimple without using an interferometric microscope.

VII. Blow Curves and Normalized Heater Power

Fig. 14 shows a series of blow curves, in which the signal power has been normalized to its maximum value. The curves were taken at a fixed hot tub temperature of 60°C and substrate temperatures ranging from 10 to 60°C.

The physical causes for the shape of the blow curves in Figs. 13 and 14 are best understood from the bubble model of Fig. 9. As the heater power increases at a fixed fluid pressure, the bubble grows in size. Hence, as the bubble grows, different sections of the bubble wall move across the waveguide's core area. For small bubbles, most of the light is reflected upwards and very little light is reflected from "IN" to "OUT" port. A first maximum in reflected light called "Foothill" is attained when the flat section above the dimple meets the waveguide. Further increasing the bubble size results in a decrease in reflected light because the bubble's inward curvature reflects a fraction of the incoming light downwards. The blow curve shows a local maximum when the center of the dimple lines up with the waveguide's location. As discussed in Section VI, the fraction of signal power reflected into the outgoing waveguide decreases again while the section of inward curvature below the center of the dimple moves across the waveguide. At some high heater power the wall dries out, and the blow curve reaches a plateau of maximum reflected optical power. This occurs for the so-called "Super Bubble," which completely fills the trench and even extends into the gap between PLC and MCC.

The blow curves in Fig. 14 are very sensitive to substrate temperature when the hot tub temperature remains fixed. This is readily understood from the fact that the bubble size is very sensitive to changes in fluid pressure at constant heater power.

In Fig. 15, we plotted the heater power $P_{\rm res}$ required at major features of the blow curve as a function of bubble to substrate temperature difference ΔT_t. The slope of the lines equals the thermal transconductance $\Gamma_{\rm bub}$, which is obtained through (3), for that particular feature or size of bubble. The features corresponding to larger bubbles possess a larger $\Gamma_{\rm bub}$, as one may expect from the discussion in Section IV.

According to (7), T_σ was found to be 1.5°C for this particular organic fluid, degassed 2-Fluorotoluene, at the given operating temperatures. In theory, all bubbles with the same curvature, or same T_σ, should be stable at zero power when $\Delta T_t = 0$ (see static bubbles in Section X). Therefore, all curves in Fig. 15 should project to zero heater power at $\Delta T_t = 0$. However, only the curve for a bubble with $\Gamma_{\rm bub} = 2.5$ mW/K indicates this projection through the origin. The data presented in Fig. 15 is known to have a measurement error in substrate temperature of about 5°C. Clearly, this is not sufficient to have the curves project to zero. Other fundamental causes of this discrepancy are unknown at this point, and probably reflect the limitations of the thermal transconductance model.

For most features of bubble operation—including "Hill," "Valley," and the "Super Bubble"— this normalization to ΔT_t, which is defined in (5), does reveal the tradeoff between heater

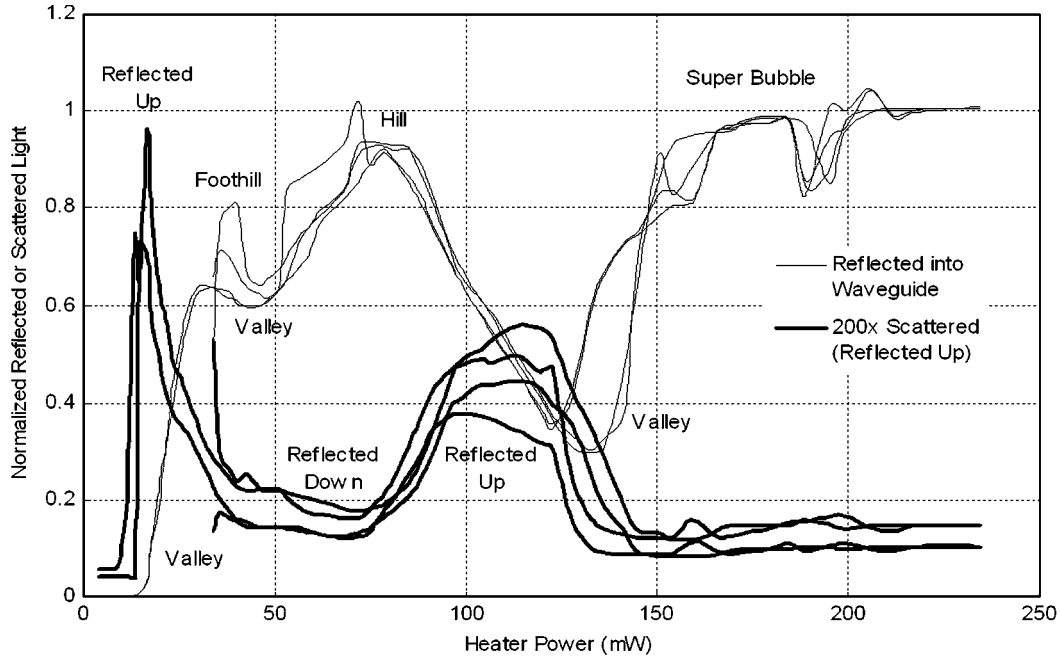

Fig. 13. Lost light and blow curve.

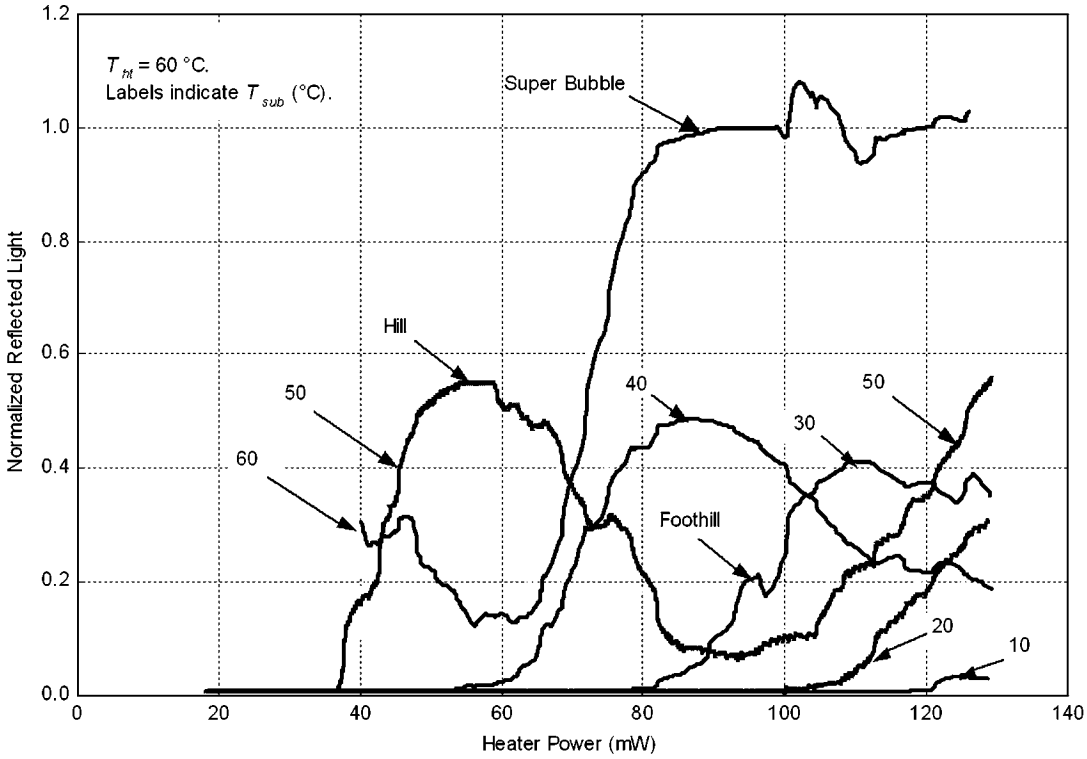

Fig. 14. Blow curves for different substrate temperatures.

power and the difference in hot tub and substrate temperature. The parameters that do not scale with this normalized heater power are vapor and liquid flux and the bubble stiffness. Fluid flux is proportional to heater power. The bubble has higher stiffness at higher fluid pressures, making its shape less sensitive to changes in heater power.

The benefit of normalizing the heater power to ΔT_t is that characterization data can be taken at one set of substrate and hot tub temperatures and still allow us to predict operation at different substrate and hot tub temperatures but with the same temperature difference. We were able to verify this property in several measurements.

VIII. Bubble Instability

The bubble tends to be sensitive to small perturbations. This causes the reflected signal to vary in amplitude over time. The major perturbations are most probably caused by contaminants in the fluid. Particle contamination is either already present in the MCC and PLC or introduced during the fluid fill process.

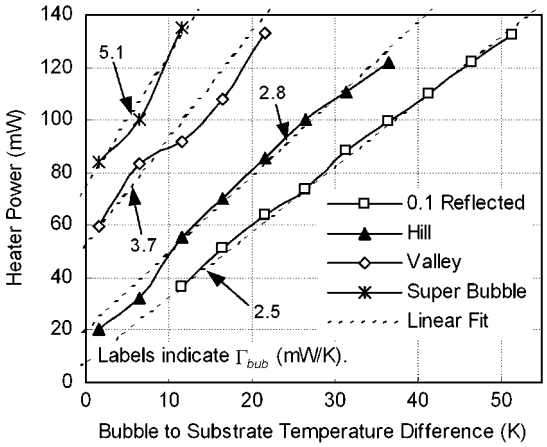

Fig. 15. Blow curve features versus ΔT_t at $T_{\rm ht} = 60°$C. "0.1 Reflected" refers to the blow curve point of 0.1 normalized reflected light before reaching the "Hill."

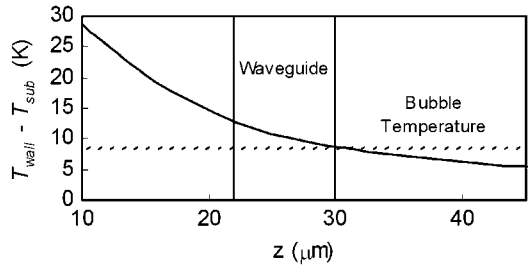

Fig. 16. Bubble and wall temperature versus z-height (z is the distance above the silicon) at $\Delta T_t = 6.5$ K and $P_{\rm res} = 100$ mW. The temperatures were extracted from a Flow3D bubble simulation.

Further process improvements are required to control and minimize such contamination.

The contaminants become concentrated in the evaporation zone due to its high fluid flux. This concentration of contaminants cuts the rate of evaporation. Hence, the bubble shrinks to accommodate the smaller evaporative flux. However, understanding the exact mechanisms of fluid contaminants and their impact on bubble dynamics requires further research.

We would expect the bubbles to be stable without the presence of contaminants. With contamination, the best reflection stability is obtained by drying out the wall of the trench at the waveguide location, which will be discussed in the following section.

IX. Drywall Operation

Because of the large amount of fluid around the bubble, the bubble temperature is very nearly at the average saturation temperature corresponding to the bubble pressure. There is very little superheat. This means that the trench wall will be wet with condensing fluid at locations where the bubble is hotter than the wall. On the other hand, if the waveguide temperature exceeds the bubble temperature, then the wall at the waveguide will be dry.

We call $T_{\rm wall} - T_{\rm bub}$ the dryness margin, where $T_{\rm wall}$ denotes the trench wall temperature at some location. Fig. 16 plots the trench wall temperature as a function of z-height along with the bubble temperature and the waveguide location. Under the operating conditions here, we will have a dry waveguide. Fluid condensation will occur right above the waveguide.

Experimentally, by looking at the reflected signal versus time, and at the stability of the reflected optical signal, we were able to determine whether the waveguide was drying out. In some cases, we observed optimally dry waveguides. In other cases, we could only achieve partially dry waveguides. The fluid gap $W_{\rm gap}$ and the presence of contaminants mainly determine the achievability of dry waveguides.

Furthermore, measurements of optical characteristics under drywall operation confirmed that the optical performance specifications of Table I in the Appendix were met—especially insertion loss and stability.

A. Bubble and Waveguide Differential Heating

Another method of keeping the waveguide mirror wall dry is to cool the bubble. A long and/or deep trench will allow the bubble to penetrate into the cooler region away from the heater. As the heater power rises, the bubble expands into the cooler regions. With a long, deep trench, the bubble never reaches the ends of the trench and $r_{\rm bub} = W_{\rm tr}/2$. Because $r_{\rm bub}$ only gets smaller as the trench narrows with depth, the bubble pressure and temperature remain nearly constant. This region is called the constant pressure or Cp region. When the bubble reaches the ends of the trench, the pressure starts to rise and $r_{\rm bub}$ decreases as the bubble pushes into the corners of the trench. This region is called the constant volume or Cv region. In this region, both bubble and wall temperature continue to increase. Fig. 17 plots bubble and wall temperature at the waveguide location as a function of side heater power. The transition from the Cp to the Cv region occurs at 17.6 mW, at which the bubble hits the top of the trench. For side heater powers greater than 12.4 mW, the wall temperature exceeds the bubble temperature and a dry waveguide results. One realizes that if the waveguide mirror wall has not dried out at the transition from Cp to Cv region, it will never dry out. As the heater power is increased, the bubble temperature rises at about the same rate as the wall temperature. Hence, the bubble will always remain hotter than the wall at the waveguide location.

Another interesting fact is that the condensing vapor heats the trench wall. As the heater power is raised, the expanding bubble will heat the wall where the fluid condenses. Thus, increased waveguide mirror dryness is a result of a competition between wall heating by conduction and condensation and bubble cooling by expansion into cooler regions.

X. Static Bubbles

It turns out that if the ambient fluid pressure is reduced by more than $\Delta p = \sigma / r_{\rm bub}$ below the vapor pressure at the given substrate temperature, the bubble will maintain itself without any power dissipation in the heater or any fluid flow in the device. This is the case when $\Delta T_t \leq 0$. However, if the pressure difference exceeds $2\sigma/W_{\rm gap}$, the bubble will expand into the gap between PLC and MCC and the device may lose all of its fluid.

This self-maintaining bubble with a stable, intermediate pressure difference is called a static or metastable bubble. It pushes into the corners of the trench. Fig. 18 shows a photo of such a

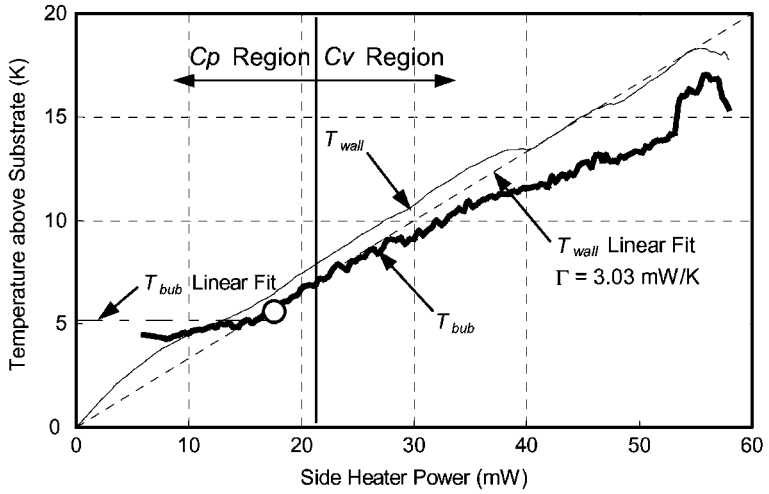

Fig. 17. Bubble and wall temperature versus side heater power. The temperature data was obtained from a 2D simulation with Flow3D.

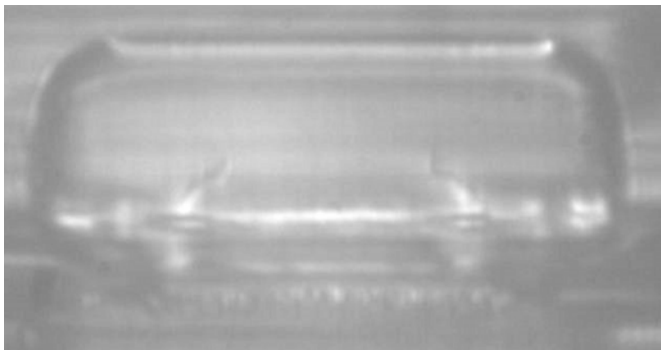

Fig. 18. Side view photomicrograph of a static bubble.

bubble. The optical reflection from this bubble is very stable. The radius of curvature everywhere is given by

$$r_{\rm bub} \geq \frac{\Delta p}{\sigma}. \tag{9}$$

This means that any minor defects in the silica mirror wall are actually filled-in by fluid and hence the reflection properties are excellent. Notice that in case of surface defects, a slightly wet wall is better than a dry one for maximizing reflection.

The change in temperature, ΔT, between the hot tub and the substrate required to maintain a static bubble follows directly from the Clausius–Clapeyron relation

$$\Delta T = \frac{\Delta p}{p} \frac{R T_{\rm bub}^2}{h_{fg}}. \tag{10}$$

The higher the liquid ambient pressure, the smaller ΔT is.

The key to making a useful switch with a static bubble is to find a method of turning it off. For instance, some kind of local pressure pulse would be required.

XI. Conclusion

In this paper, we have shown how simple analytic models, Flow3D finite difference modeling, and a number of experimental observations have helped us to explain the behavior of the opto-fluidic bubbles encountered in Agilent's Optical Switch.

In summary, our research on optical switch bubbles revealed

1) the value of simple thermal conductance modeling in elucidating the basic bubble energetics;
2) the importance of bubble temperature in determining bubble behavior;
3) the convenience of normalizing the heater power by the difference between bubble and substrate temperature;
4) the consequence of the details of wall condensation in determining the reflective properties of wet wall bubbles;
5) the significance of wall temperature minus bubble temperature in determining whether the wall becomes dry;
6) the drywall operation of the optical switch to meet all optical performance specifications;
7) the existence and potential value of very stable, static bubbles.

TABLE I
Optical Performance Specifications

Parameter	Symbol	Specification	Units
optical passband (wideband)		1260-1360, 1480-1580	nm
insertion loss	*IL*	8.5	dB
uniformity	*U*	2.6	dB
wavelength flatness	*WF*	0.2	dB
stability		0.5	dB
repeatability		0.05	dB
polarization dependent loss	*PDL*	0.2	dB
crosstalk	*XT*	-55	dB
directivity	*D*	55	dB
return loss	*RL*	55	dB
differential group delay	*DGD*	0.2	ps
maximum allowable optical power		25	dBm
switching time		10	ms

Appendix

See Tables I–III.

TABLE II
NOMENCLATURE

Symbol	Quantity	Units
A_{bubE}	evaporating area of the bubble	m^2
C	accommodation coefficient	
Ca	capillarity	
Cp	constant pressure region	
Cv	constant volume region	
h_{fg}	enthalpy of evaporation	J/kg
m	condensing vapor flux	kg/(s·m^2)
M	molecular weight	kg/kgmole
p	vapor pressure of the fluid	Pa
p_{bub}	vapor pressure inside the bubble	Pa
P_v	vapor pressure inside the bubble	Pa
P_l^{sat}	saturation pressure of the liquid	Pa
P_{res}	heater power	W
R	gas constant	J/(kg·K)
r_{bub}	bubble radius of curvature	m
T_{bub}	bubble temperature	°C
T_C	condensing surface temperature	°C
T_E	evaporating surface temperature	°C
T_{hl}	hot tub temperature	°C
T_{liq}	liquid temperature	°C
T_v	vapor temperature inside the bubble	°C
T_{sub}	substrate temperature	°C
T_{wall}	trench wall temperature	°C
T_{wg}	waveguide wall temperature	°C
T_σ	equivalent temperature difference that generates pressure to overcome surface tension	°C
W_{tr}	trench width	m
W_{gap}	gap width	m
Δp	difference in pressure across the bubble wall	Pa
ΔT	difference in temperature between hot tub and substrate	°C
ΔT_t	bubble to substrate temperature difference	°C
Γ	thermal transconductance	W/K
Γ_{bub}	heater to bubble thermal transconductance	W/K
ν	kinematic viscosity	m^2/s
σ	surface tension	N/m

TABLE III
PHYSICAL PROPERTIES OF 2-FLUOROTOLUENE

Parameter	Symbol	Value	Units
liquid density	ρ	1001	kg/m^3
liquid heat capacity	c_p	1540	J/(kg·K)
liquid thermal conductivity	κ	108	W/K
liquid viscosity	ν	$0.64\cdot10^{-3}$	Pa·s
fluid-solid contact angle	θ_c	0	°
surface tension	σ	$27.64\cdot10^{-3}$	N/m
temperature coefficient of surface tension	$\frac{d\sigma}{dT}$	$-0.114\cdot10^{-3}$	N/mK
ratio of specific heats	γ	1.08	
specific heat of vapor (at constant volume)	c_v	944	J/(kg·K)
enthalpy of evaporation	h_{fg}	$321.4\cdot10^3$	J/kg
vapor pressure (at 25 °C)	p	$3.25\cdot10^3$	Pa
accommodation coefficient	C	2	

ACKNOWLEDGMENT

The authors would like to credit the work of and many discussions with V. Ajaev and Prof. B. Homsy of the University of California, Santa Barbara, plus the very large amount of work done by their colleagues in the "Champagne" Optical Switch project at Agilent Technologies. Flow Sciences supplied the Flow3D simulation software, which was critical to the understandings obtained in our research.

REFERENCES

[1] M. Blander and J. L. Katz, "Bubble nucleation in liquids," in *AIChE J.*, 1975, vol. 21, no. 5, pp. 833–848.
[2] W. Chen, R. Mei, and J. F. Klausner, "Vapor bubble growth in heterogeneous boiling," in *Convective Flow Boiling*, J. C. Chen, Ed. Washington, DC: Taylor and Francis, 1996, pp. 91–98.
[3] W. M. Rohsenow, J. P. Hartnett, and Y. I. Cho, *Handbook of Heat Transfer*, 3rd ed. New York: McGraw-Hill, 1998.
[4] Y. S. Kao and D. B. R. Kenning, "Thermocapillary flow near a hemispherical bubble on a heated wall," *J. Fluid Mech.*, vol. 53, pt. 4, pp. 715–735, 1972.
[5] S. DasGupta, J. A. Schoenbert, I. Y. Kim, and P. C. Wayner, Jr., "Use of the augmented Young-Laplace equation to model equilibrium and evaporating extended menisci," *J. Colloid Interface Sci.*, vol. 157, pp. 332–342, 1993.
[6] M. S. Plesset and A. Prosperetti, "Flow of vapour in a liquid enclosure," *J. Fluid Mech.*, pp. 433–444, 1976.
[7] V. S. Ajaev and G. M. Homsy, "Steady vapor bubbles in rectangular micro channels," *J. Colloid Interface Sci.*, vol. 240, no. 1, pp. 259–271, Aug. 2001.

John J. Uebbing (M'88) was born in Chicago, IL, in 1937. He received the B.S.E.E. degree from the University of Notre Dame, Notre Dame, IN, in 1960, the M.S.E.E. degree from the Massachusetts Institute of Technology, Cambridge, in 1962, and the Ph.D.E.E. degree from Stanford University, Stanford, CA, in 1967.

He has worked in optoelectronics and electrooptics for his entire career. His first position was at Varian Associates, Palo Alto, CA. In 1973, he went to work for Hewlett-Packard, Palo Alto, CA, which became Agilent Technologies, Santa Clara, CA, in 1999, and then for Lumileds Lighting, San Jose, CA. He did product development for LED displays, fiber optic modules, bar code sensors, motion sensors, liquid crystal displays, LED print bars, and fiber optics switches. He is currently working as an optical consultant. He is the holder of 22 U.S. patents in the optoelectronics field.

Dr. Uebbing has been an SID member.

Stephan Hengstler (S'99–M'02) was born in Villingen-Schwenningen, Germany, in 1974. He received the M.S. degree in electrical engineering and information technology from the University of Karlsruhe "Fridericiana," Karlsruhe, Germany, and the M.S. degree in electrical engineering from the University of Massachusetts, Dartmouth, both in 2001.

From 1997 to 1999, he was a Student Research Assistant at the Karlsruhe Research Center for Technology, Karlsruhe, Germany. In 2001, he joined Agilent Technologies, Inc., Santa Clara, CA, as a Hardware Design Engineer R&D. Since 2005, he has been with the Biosensor Solutions Division at Avago Technologies, San Jose, CA. His current and previous research interests include wireless *ad-hoc* and sensor networks, spread spectrum communications, time-frequency signal processing, and optical switching technology.

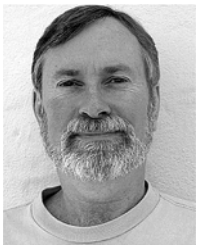

Dale Schroeder was born in Carroll, IA, in 1950. He received the B.S. degree in electrical engineering from the University of Iowa, Ames, in 1980.

He joined Westinghouse Electric Company, Iowa City, IA, in 1973 as a Designer of optical mark reading equipment. In 1980, he joined Hewlett-Packard, Santa Clara, as a Hardware Design Engineer R&D, transitioned to Agilent Technologies, Inc. in 1999, and joined Agilent Laboratories, Santa Clara, CA, as a Master Technical Contributor in 2002. His current and former research interests include high precision analog electronics, digital signaling, optics, micro fluidics, and nanoscale technology.

Shalini Venkatesh (M'92–SM'00) was born in Coimbatore, India, in 1954. She received the B.Sc. degree (honors physics) and the Ph.D. degree (medical physics) from the University of Aston, Aston, U.K., in 1976 and 1980, respectively.

She worked as a Researcher in a number of branches of medical physics before entering the field of fiber optics in 1984, first as a Research Fellow at Strathclyde University, U.K., and then as the Schlumberger Lecturer in Optical Sensors at University College London, U.K. She joined Hewlett-Packard Laboratories, Palo Alto, CA, in 1988, transitioned to Agilent Laboratories in 1999, and currently works as a Senior Research Scientist at Avago Technologies, San Jose, CA. Her current interests include solid-state illumination and image sensor applications.

Dr. Venkatesh is a member of the Institution of Engineering and Technology.

Rick Haven was born in Bridgeport, CT, in 1953. He received the B.A. degree in mathematics and the B.S. degree in mechanical engineering from the University of Connecticut, Storrs, in 1975, and the S.M. and Ph.D. degrees in mechanical engineering from the Massachusetts Institute of Technology, in 1977 and 1980, respectively.

He joined Hewlett-Packard, Palo Alto, CA, in 1980, transitioning to Agilent Technologies, Santa Clara, CA, in 2000. He has worked in optoelectronics, medical products, HP Labs, and electronic assembly development (Palo Alto, CA; Andover, MA; and Boeblingen, Germany). He is currently working at Agilent Labs on the New Business Creation team, Santa Clara, CA. His current interests include new business creation, renewable energy, image processing, and thermal management.